The instability and breaking of long internal waves

By CARY D. TROY AND JEFFREY R. KOSEFF

Environmental Fluid Mechanics Laboratory, Stanford University, Stanford, CA 94309-4020, USA

Laboratory experiments are carried out to determine the nature of internal wave breaking and the limiting wave steepness for progressive, periodic, lowest-mode internal waves in a two-layer, miscible density stratification. Shoaling effects are not considered. The waves investigated here are long relative to the thickness of the density interface separating the two fluid layers. Planar laser-induced fluoresence (PLIF) flow visualization shows that wave breaking most closely resembles a Kelvin–Helmholtz shear instability originating in the high-shear wave crest and trough regions. However, this instability is strongly temporally and spatially modified by the oscillations of the driving wave shear. Unlike a steady stratified shear layer, the wave instability discussed here is not governed by the canonical $Ri = 1/4$ stability limit. Instead, the wave time scale (the time scale of the destabilizing shear) imposes an additional constraint on instability, lowering the critical Richardson number below 1/4. Experiments were carried out to quantify this instability threshold, and show that, for the range of wavenumbers considered in this study, the critical wave steepness at which the wave breaking occurs is wavenumber-dependent (unlike surface waves). The corresponding critical wave Richardson numbers at incipient wave breaking are well below 1/4, in consonance with a modified instability analysis based on results from stratified shear flow instability theory.

1. Introduction

Breaking internal waves are known to play a crucial role in the transport of mass and momentum in lakes (Hodges *et al.* 2000; Boegman *et al.* 2003), the ocean (Gregg 1987; Gregg, Winkel & Sanford 1993), and the atmosphere (Fritts 1989; Scinocca 1995). The energy and mass transfers associated with breaking internal waves are important, usually sub-grid scale processes that must be accurately modelled in regional and global ocean and atmosphere numerical models. The use of oceanic and atmospheric microstructure measurements to infer diapycnal mixing associated with breaking internal waves also requires the accurate parameterization of internal wave breaking events. Crucial to the accurate parameterization of these events is a thorough understanding of the instabilities resulting in internal wave breaking.

This paper describes the results of laboratory experiments investigating progressive monochromatic internal wave breaking in a two-layer-type density stratification. The experiments demonstrate conclusively, for waves that are long relative to the interfacial thickness, that wave breaking occurs due to a modified Kelvin–Helmholtz ('K-H') instability. The work aims to resolve two fundamental issues related to breaking internal waves: (i) the critical amplitude at which a progressive monochromatic inter-facial wave will break and (ii) the mechanism(s) by which the wave becomes unstable
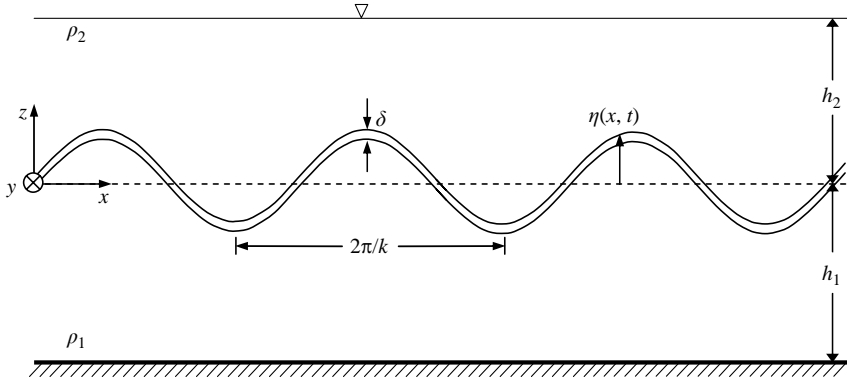
FIGURE 1. Schematic of progressive long internal wave flow.

and breaks. This paper is laid out as follows. A brief review of internal wave breaking and relevant studies is presented in §2. Section 3 describes the laboratory facilities and techniques used for the wave breaking experiments; the results of the experiments are presented in §4. In §5, the results are discussed in the light of modified stratified shear flow stability analysis, and conclusions are presented in §6.

2. Background

The present discussion focuses on periodic internal gravity waves that are long relative to the vertical scale of variability associated with the background density stratification; an excellent review on shorter waves is given in Staquet & Sommeria (2002). The density stratification supporting internal waves in much of the Earth's oceans, lakes and atmosphere can be approximated as a two-layer stratification, in which a well-mixed upper layer is separated from a denser, homogeneous bottom layer by a thin region (Wessels & Hutter 1996; Michallet & Ivey 1999). The parameter $g' = g\Delta\rho/\rho_0$ describes the reduced gravity that provides the restoring force supporting the waves in the system, where $\Delta\rho = \rho_1 - \rho_2$ is the density difference between the lower (ρ_1) and upper (ρ_2) fluid layers, and $\rho_0 = (\rho_1 + \rho_2)/2$ is the average density. In this case, the density distribution can be effectively approximated by a hyperbolic tangent profile:

$$\rho(z) = \rho_0 - \frac{\Delta\rho}{2}\tanh(mz). \tag{1}$$

The hyperbolic tangent profile is used here in lieu of an error function profile because of the existing analytical work on the latter profile (Thorpe 1968*c*, 1978); however, Thorpe (1971) showed that the stability properties of both profiles are similar.

The work described herein focuses on horizontally propagating lowest mode monochromatic internal waves travelling on the density interface. A schematic of the flow is presented in figure 1. Specifically, the threshold for wave instability and the nature of wave breaking are examined here for waves long relative to the interfacial thickness, or rather waves having small $k\delta$, where $k = 2\pi/\lambda$ is the horizontal wavenumber and δ is a measure of the 99% density interface thickness, here computed from the vertical density profile $\rho(z)$ as

$$\delta = z\{\rho = 0.99(\rho_0 - \rho_2)\} - z\{\rho = 0.99(\rho_1 - \rho_0)\}. \tag{2}$$

The 99 % interfacial thickness δ can be related to the length scale associated with the density profile (1) as

$$\delta = \frac{5.3}{m}. \tag{3}$$

This conversion is provided for ease of comparison with other work on stratified shear layers, where $1/m$ or $\Delta\rho/(\partial\rho/\partial z)_{z=0} = 2/m$ are sometimes used as the normalizing length scales.† This definition of δ corresponds to that used by Fringer & Street (2003) in their numerical experiments.

In this paper, horizontal boundary effects that induce wave shoaling are not considered; rather, the focus is on 'deep' waves (kh_1, kh_2 large, where h_1 and h_2 are the lower and upper layer depths, respectively). The lowest-order description of the interfacial distortion $\eta(x, t)$ induced by the progressive wave train is $\eta(x, t) = a\cos(kx - \omega t)$, where a is the wave amplitude.

Phillips (1966, p. 185) argued that lowest-mode progressive internal wave breaking would occur in the form of a shear instability induced by the strong local vertical shear present at the wave crests and troughs. To lowest order, the wave-induced gradient Richardson number at these locations is

$$Ri_w \equiv \left.\frac{N^2}{|\partial U/\partial z|^2}\right|_{z=0, x=crest/trough} \tag{4}$$

$$\approx \frac{k\delta}{5.3(ka)^2}. \tag{5}$$

Here

$$N(z) = \sqrt{\left(\frac{-g}{\rho}\right)\bigg/\frac{\mathrm{d}\rho}{\mathrm{d}z}}$$

is the local Brünt–Väisälä frequency (rad s^{-1}) describing the background stratification, and $\partial U/\partial z$ is the vertical shear of the wave-induced horizontal velocity $U(x, z, t)$. The parameter ka is the wave steepness. The estimate (4) is obtained using the normal-mode solution derived by Thorpe (1968) for periodic lowest-mode internal waves in a hyperbolic-tangent (two-layer) density profile. This approximation holds well for low values of $k\delta$ and $(kak\delta)$, but requires correction at higher $(kak\delta)$ Fringer & Street (2003). Another estimate for the interfacial Richardson number at the wave crests and troughs is $Ri_w = k\delta/2(ka)^2$, which is obtained by using the two-layer interfacial deep wave solutions (e.g. Turner 1973, p. 14), and assuming that the shear and density variation both occur over a common vertical scale δ. This estimate is an overprediction of the mid-interface Richardson number, but is convenient to use since it can easily be obtained from the linear, irrotational two-layer wave solutions. It differs by a constant from that of Thorpe (1968), (4), due to differences in the definitions of δ between the two-layer approximation and the continuously stratified formulation. Regardless of the specific formulation used, the Richardson number at the wave crests and troughs is determined fully by the wave parameters ka and $k\delta$; for this reason it is referred to here as the 'wave Richardson number' and denoted Ri_w. We refer to the time-varying mid-interface Richardson number as Ri_0. The relationship between the two is explained fully in §5.

---

† For an error function profile $\rho(z) = \rho_0 - (\Delta\rho/2\rho_0)\mathrm{erf}(\beta z)$, the 99 % interfacial thickness is $\delta = 3.7/\beta$, and $\Delta\rho/(\partial\rho/\partial z)_{z=0} = 2/\beta$.

The stability of a steady, parallel, two-dimensional, inviscid, stratified shear flow to infinitesimal perturbations is guaranteed if the Richardson number is everywhere greater than 1/4 (Miles 1961; Howard 1961). If the Richardson number is anywhere below 1/4, then instability is possible, but not guaranteed. For coincident, equal-thickness hyperbolic tangent density and velocity profiles, Hazel (1972) showed that the flow stability could be phrased in terms of the mid-point Richardson number, and that the flow was unstable to certain perturbations if the mid-point Richardson number fell below 1/4 Hazel (1972) Thorpe (1968c) showed that the flow at the crests and troughs of lowest-mode long interfacial waves is described well by the hyperbolic-tangent profiles. Neglecting unsteadiness, the stability of the high-shear crest and trough regions of long progressive interfacial waves can, similarly, be phrased in terms of the wave Richardson number Ri_w, the mid-point Richardson number (4). The simple application of a $Ri = 1/4$ instability criterion with either of the Ri_w estimates given earlier yields that the critical wave steepness ka_{crit}, the steepness above which wave breaking occurs, should be wavenumber-dependent and scale as $ka_{crit} \sim (k\delta)^{1/2}$. The constant of proportionality will be particular to the Ri_w estimate used. This wavenumber dependence of the limiting wave steepness for finite-thickness interfacial waves is an important distinction from infinitesimal-thickness interfacial gravity waves (e.g. air–water waves), for which the limiting steepness is independent of wavenumber. However, the application of the $Ri = 1/4$ criterion to finite-amplitude interfacial waves is questionable, since the flow is unsteady. Thorpe (1968) hypothesized that for high-frequency internal waves, shear-induced internal wave breaking could occur at wave crests and troughs only if the instability time scale was suitably smaller than the wave period. This idea is expanded in §5.

Orlanski & Bryan (1969), Long (1972), Holyer (1979), Thorpe (1978), and others have argued that progressive internal wave breaking occurs due to convective instability. Thorpe's (1978) finite-amplitude normal mode solutions suggested that convective breaking would occur before shear instability for progressive waves in an asymmetric two-layer stratification, with a limiting wave steepness of $ka = 0.35$ for a wave with $k\delta = 0.56$. Holyer (1979), for Boussinesq infinitesimal-interface waves, calculated a convective wave breaking steepness of $ka = 1.1$, substantially larger than $ka = 0.443$, the steepness at which progressive deep air–water interfacial waves break (Stokes 1849). However, the effect of a finite-thickness interface was not considered in the calculations. The convective breaking criterion, $U > c_p$, where the wave-induced velocity U exceeds the wave phase speed c_p, can be phrased in terms of a critical steepness formulation $ka > ka_{crit}$ since the maximum wave-induced velocity is $U \sim a\omega$ and $c_p = \omega/k$. Experiments by Grue *et al.* (2000) showed that solitary waves in two-layer stratifications break when the wave-induced fluid velocity approached the wave phase speed. Standing internal waves in two-layer stratifications have also been shown to break due to a convective instability Thorpe (1968). Observations and modelling of long internal waves in the atmosphere have also pointed to convective instability as the cause of wave breaking (Hecht *et al.* 1997; Fritts *et al.* 1997).

It is also thought that the presence of a weak background shear reduces the wave slope at which long internal wave breaking occurs. Breaking internal wave visualizations in the ocean thermocline by Woods (1968) verified that wave breaking due to shear instability could be enhanced by the presence of a weak background shear. Thorpe's (1978) finite-amplitude two-layer wave calculations and laboratory experiments also showed that the threshold slope for wave breaking was reduced in the presence of a background shear. The calculations predicted that with or without background shear, wave breaking would take place due to a convective instability

for the wavenumbers considered. Stastna & Lamb (2002) showed that the nature of non-uniform background flows is important in determining the limiting amplitude and breaking mechanism of two-layer internal solitary waves. Critical layers are also important regions where background shear dictates internal wave instability (Lin *et al.* 1993; Winters & D'Asaro 1994), but they are not immediately relevant to the long wave discussion here since in that case the wavelength shortens to a scale on the order of the vertical scale of the stratification.

Antenucci & Imberger (2001) and Boegman *et al.* (2003) observed high-frequency internal waves in lakes near internal Kelvin wave fronts. These high-frequency waves had wavenumbers and frequencies that agreed well with those predicted by numerical solutions to the Taylor–Goldstein equation for the observed background density and velocity profiles, suggesting that shear instability resulted from the enhanced shear associated with the internal Kelvin waves.

Internal wave–internal wave interactions are thought to be an important energy transfer mechanism and possible wave breaking cause in polychromatic internal wave fields Thorpe (1975). However, first-mode progressive internal waves cannot have an $O(ka)$ resonant triad with other first-mode internal waves (Thorpe 1966; Davis & Acrivos 1967; Phillips 1966, §5.4). Davis & Acrivos (1967) showed analytically and experimentally that, for two-dimensional progressive interfacial waves, the most likely triad to form in two-layer stratifications was composed of a progressive first-mode wave, a progressive second-mode wave, and a third, oppositely travelling third mode-wave.

The work most immediately relevent to the present study is that of Fringer & Street (2003), who carried out high-resolution numerical simulations of breaking monochromatic interfacial waves in tandem with the laboratory studies described here. They found that moderate-length internal waves ($0.31 < k\delta < 0.56$) broke due to a two-dimensional shear instability, while shorter waves ($k\delta > 0.56$) broke due to a mixed shear–convective instability, and that the critical steepness for all waves was wavenumber-dependent, ranging from $ka = 0.75$ to 1.05. Our work complements their study for the low-$k\delta$ range ($k\delta < 0.3$).

The results presented here address the question of the nature and threshold of wave breaking for non-shoaling progressive two-layer internal waves away from horizontal boundaries. In the absence of a background mean shear, a progressive deep monochromatic interfacial wave in a two-layer density stratification, with a finite-thickness interfacial region, is fully characterized by the set of parameters $\{a, k, \delta, \nu, \kappa, g'\}$. The parameter ν is the fluid kinematic viscosity and κ is the diffusivity of the stratifying scalar. The dispersion relation sets the wave frequency ω, and the wave-induced velocities are determined by the entire parameter set. Regardless of the instability mechanism–convective or shear–the critical wave steepness ka_{crit} at which progressive interfacial waves break can be phrased as having the functional dependence

$$ka_{crit} = F(k\delta, Re_w, Sc), \qquad (6)$$

where Re_w is the wave Reynolds number (defined later). The parameter $Sc \equiv \nu/\kappa$ is the Schmidt number, giving the ratio of momentum diffusivity (ν) to the diffusivity of the stratifying scalar (κ). The primary focus of this paper is illuminating the dependence of ka_{crit} on $k\delta$ for low values of $k\delta$ (long waves), low-to-moderate Re_w, and fixed $Sc \approx 700$ (salt). The wave breaking criterion (6) can be phrased equivalently in terms of a critical wave-induced Richardson number, $Ri_{w,crit}$, below which the wave will
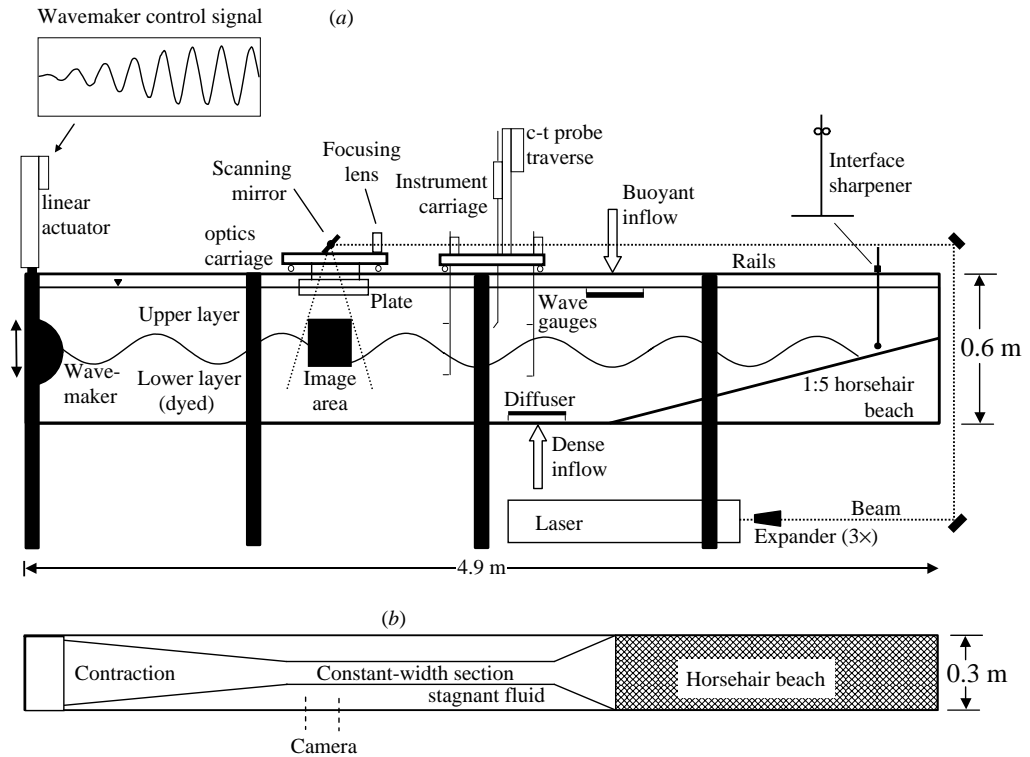
FIGURE 2. Schematic of laboratory facility and instrumentation used in internal wave experiments: (*a*) side view, (*b*) plan view.

break. Then $Ri_{w,crit}$ replaces ka_{crit}, since the parameters ka and $k\delta$ fully determine Ri_w, (4).

3. Laboratory experiments

Laboratory experiments were designed to force progressive monochromatic internal waves to breaking, allowing the measurement of the wave amplitude at wave breaking and the detailed visualization of the wave breaking events. Following a comment by Turner (1973, p. 126), a laterally contracting channel was used to force waves to breaking. The approach used here is similar to that used by Ramberg & Griffin (1987) in which monochromatic surface water waves were forced to breaking through a lateral channel contraction.

3.1. *Experimental facility*

The laboratory experiments were carried out in the Stanford University Environmental Fluid Mechanics Laboratory internal wave facility shown in figure 2. The facility is an enclosed rectangular tank constructed of modular steel frame supports and 2.5 cm thick clear Plexiglas walls, with dimensions 488 cm long, 61 cm tall, and 30 cm wide. The main features of the tank include a vertically oscillating ('plunger' type) interfacial wavemaker, a slideable carriage holding mounted instruments, another sliding carriage with a mounted camera and laser optics to generate a vertical laser light sheet for flow imaging, a density interface sharpening device, a synthetic horsehair beach to prevent wave reflections, and surface and bottom diffuser plates for filling. Additionally, for

the present experiments, laterally contracting sidewalls were placed in the tank to promote wave growth. The tank is housed in a constant-temperature room capable of maintaining the temperature to within $\pm 1\,^{\circ}$C.

3.1.1. *Stratification and density measurement*

The fluid density stratification used in the experiments is a two-layer saline stratification with a thin, continuously varying interfacial region separating the two fluid layers. The densities of the fluid layers are prepared in separate storage reservoirs to the desired values using an Anton-Parr density meter (model DMA 4500). For all of the laboratory experiments, a density difference of $\Delta\rho/\rho_0 = 3.0 \pm 0.1\,\%$ was used, where $\Delta\rho = \rho_1 - \rho_2$ is the density difference between the lower and upper layers, and $\rho_0 = (\rho_1 + \rho_2)/2$ is the average density. To fill the tank, the fresher, upper layer is first introduced into the tank; then, very slowly, the saltier, lower layer is injected below the fresh layer. A diffuser plate is positioned at the tank inlet to minimize mixing during the filling process.

Vertical profiles of fluid density are obtained by traversing a conductivity temperature probe (Precision Measurements Engineering model 125) through the water column at $10\,\mathrm{cm\,s}^{-1}$. This probe is frequently calibrated against the Anton-Parr density meter to eliminate calibration drift during experiments.

To maintain the desired thin density interface between the two homogeneous fluid layers, fluid is selectively withdrawn from the interfacial region prior to an experiment using a thin slotted pipette, attached to a pump, and positioned at the density interface. Following an experiment, during which the interface thickens, the interface is re-sharpened to the desired thickness. Water is then added through the bottom and top diffuser plates to maintain the fluid layer depths. Through a combination of the interfacial sharpening and layer refilling, as many as 40 separate experimental runs can be performed for a given experiment, at which point the fluid in the two large reservoirs feeding the tank is usually exhausted. Typically the fluid layers are maintained at $h_1 = h_2 = 28 \pm 0.2\,\mathrm{cm}$ and the interfacial thickness is sharpened to a thickness $\delta = 1.00 \pm 0.05\,\mathrm{cm}$ prior to an experimental run. The interfacial thickness was measured by fitting the hyperbolic tangent profile (1) to the profiles and using (3). Figure 3 shows sample density profiles demonstrating the repeatability of the sharpening and refilling technique for generating the initial experimental stratification. The Brünt–Väisälä frequency associated with this density interface, $N = \sqrt{g'/\delta}$, sets the maximum frequency of interfacial waves that can exist in the stratification.

3.1.2. *Laterally contracting channel*

In order to force monochromatic wave trains to breaking, an external wave growth mechanism was required to overcome the damping effects of viscosity. A laterally contracting channel section was placed in the tank to force wave growth with distance away from the wavemaker; this channel contraction was followed by a constant-width test section, which was followed by a brief expansion section at the wave damping beach (figure 2). The lateral contraction and the test section were constructed of thin transparent Plexiglas sheets fixed at the bottom and top of the facility. It was found that a more severely contracting channel was necessary to overcome the large damping effects of viscosity, which limited the experiments to investigations of longer (low-$k\delta$) waves. The width of the constant-width test section was chosen with care because, as Thorpe (1987) showed, sidewall turbulence in narrow laboratory experiments involving stratified fluids can cause spurious effects and lead to difficulty in the interpretation of results. The width of the constant-width section was chosen
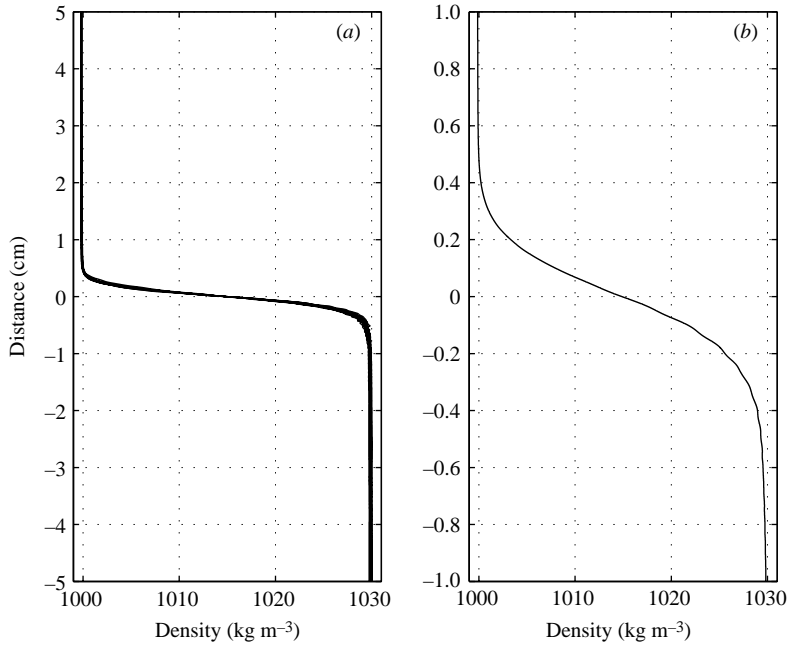
FIGURE 3. Pre-experiment vertical density profiles following the interface sharpening technique. (*a*) The profiles from 10 separate experimental runs; (*b*) the average profile, at enlarged scale.

iteratively to be sufficiently wide that sidewall turbulence contamination was negligible for the wave frequencies described in this paper. This could be seen by looking at the tank from above and viewing the index-of-refraction fluctuations near the sidewalls. For test sections that were too narrow, or wave frequencies that were too high, sidewall turbulence migrated to the centre of the test section, and contaminated the flow in the test section before wave instability could occur. After several iterations, the contraction shown in figure 2 was chosen for the experiments. The walls smoothly contract laterally from 30 cm wide to 10 cm wide over a horizontal length of 140 cm, followed by an expansion section. To prevent wave reflections from contaminating the waves, a 1:6 sloping synthetic horsehair beach was placed at the far end of the tank. No effects of wave reflection were observed during the experiments.

3.1.3. *Wave generation*

Waves are generated with a semi-cylindrical 'plunger' type wavemaker positioned at the interface between the two fluid layers. The wavemaker head was constructed from a piece of bisected, 27.5 cm diameter PVC piping. To generate waves, a linear actuator (Industrial Devices Corporation model EC-2) vertically oscillates the wavemaker head in proportion to a time-varying analog voltage control signal that is generated by a computer. The shape of the waves was checked using ultrasonic wave gauge measurements (for details on the probe see Michallet & Barthelemy 1997), and no undesired wave anomalies were found to be present in the monochromatic wave trains generated. At higher frequencies and large wavemaker stroke amplitudes, some mixing was generated by the wavemaker, and for these cases, care was taken to ensure that this mixed fluid did not reach the test section during the times of interest for the experiment. The practical upper frequency limit for wave generation in the present experiments was set not by the Brünt–Väisälä frequency of the density interface,
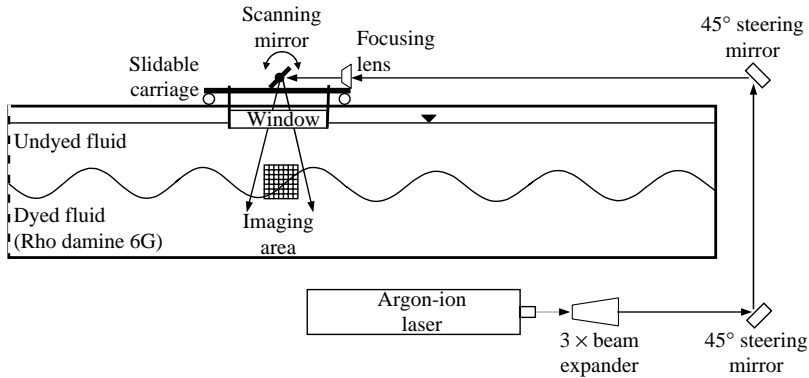
FIGURE 4. Flow imaging system. Not shown is the wavemaker or the horsehair beach.

but by viscous damping, primarily from the sidewall boundary layers, which quickly damped the high-frequency waves (for details see Troy 2003). For these reasons, the laboratory experiments were limited to the parameter range $0.05 < k\delta < 0.3$.

A constant-frequency, amplitude-modulated signal was used to drive the wavemaker motion. The signal amplitude was ramped linearly in time from zero to a maximum amplitude such that at some point in time, at the beginning of the test section, which was the spatial location of the maximum wave amplitude in the channel, the wave would become unstable. This allowed a single experiment to determine the critical wave amplitude for a given wavenumber, provided that the maximum wave amplitude occurring in the channel contraction over the course of the experiment was large enough to induce wave breaking. This technique also allowed the camera to be positioned at the location where the wave would first become unstable, the beginning of the constant-width test section, ensuring that the first wave breaking event would be observed by the camera. The amplitude was increased linearly generally over 5–10 wave periods, which was chosen to be long enough that no additional wave components would be introduced into the tank, but short enough that the wave would pass quickly through the instability transition, allowing the transition to be easily identified.

3.1.4. *Flow imaging*

Quantitative flow imaging was done using planar laser-induced fluorescence (PLIF). The PLIF images were used to track the density interface, measure wave and billow properties and to capture images of the wave instability. For PLIF experiments, the lower, saltier fluid layer is seeded with laser-fluorescing dye, Rhodamine 6G, in the same manner as the stratifying agent (salt). The laser-induced fluorescence of the Rhodamine can then be used as a surrogate for the salinity of the fluid since salt and Rhodamine have similar diffusivities. An argon-ion laser (Coherent Innova 305), set to 514 nm emission, is mounted below the tank as shown in figure 4. The emitted beam is routed around the tank and focused onto a scanning mirror that sweeps the beam across the imaging area, during which time the camera shutter is opened, creating an image of the fluorescing fluid. High-resolution pictures were taken with a 1024 by 1024 12-bit greyscale digital camera (Silicon Mountain Designs); image sizes ranged from 15 to 20 cm, setting the single pixel resolution at 0.15 to 0.20 mm. The focused laser beam, at the centre of the image, has a diameter of less than 0.5 mm, which sets the transverse resolution of the images. A typical scan time for the images is 15 ms,

and frames were typically acquired at between 7.5 and 10.0 Hz. Images are corrected for attenuation and calibrated by comparing an image of the static, pre-experiment interface with a vertical density profile taken at the same time. For selected imaging experiments, the index of refraction was matched between the two fluid layers in order to eliminate unwanted image aberrations due to index-of-refraction fluctuations. This was done by seeding the upper fluid layer with 70 % isopropyl alcohol, following standard techniques (McDougal 1979; Alahyari & Longmire 1994; Daviero, Roberts & Maile 2001). Additional details on the experimental methods and instrumentation can be found in Troy & Koseff (2005).

4. Results

4.1. *Breaking mechanism*

The results of the internal-wave-breaking flow visualization experiments will now be described in detail. These experiments demonstrated that the breakdown mechanism for long interfacial waves ($0.05 < k\delta < 0.3$) was a modified shear instability, with characteristic K-H billow roll-up and collapse. Waves having amplitudes beyond the threshold amplitude for instability appeared to become unstable to a vigorous, strongly spatially and temporally modfied K-H instability originating at the high-shear wave crest and trough regions.

The evolution of long internal wave breaking, as observed in the laboratory experiments, is described from the point of view of a stationary observer at the location of the fixed camera, which was placed at the beginning of the constant-width test section in the channel ($x = 140$ cm). This is the location in the channel where the wave amplitudes were largest and thus the location where wave breaking first occurred. From this perspective, since the amplitude of the wave forcing was slowly increasing in time, one observed the passage of waves with temporally increasing amplitude. Typical results from the flow visualization experiments are presented in the image sequences shown in figure 5. Time has been normalized with the wave period T, with time $t/T = 0$ corresponding to the passage of the first wave crest in the wave train.

Locally, as the wave amplitude grew in time, the first sign of instability was the development of small interfacial disturbances, appearing as small first-mode distortions of the interface, that formed in the crests and troughs of the waves. Figure 5 shows the development of the disturbances in the crests ($t/T = 0, 0.125$) and troughs ($t/T = 0.375$) of the wave. These disturbances develop slightly behind ($-x$) the wave crests, for the forcing used in this experiment, and grew slightly in amplitude as the wave passed through them. The disturbances appeared to drift very weakly in the direction of wave propagation, but quantifying the drift was difficult in the midst of the interfacial motion associated with wave passage. For the first few wave crests and troughs following their initial observation the interfacial disturbances, simply appear, grow slightly with the passage of the wave, disappearing by the arrival of the next wave node, and then reappearing in the next wave trough/crest. The disturbances were slightly more prevalent in wave troughs than crests. Between 1 and 4 disturbances formed in the wave crests and troughs during this phase, with larger numbers of disturbances forming at later times, when wave amplitudes were close to the breaking amplitude. The behaviour of the interfacial disturbances in this stage is consistent with a disturbance that has a non-zero growth rate, but a growth rate that is of insufficient magnitude to lead to overturning in the time scale of the applied wave shear.

As the waves grew further in amplitude, the growth of the interfacial disturbances in one crest/trough passage period increased, until a point at which a thin wisp of fluid was sometimes sheared off of a disturbance into the upper fluid layer, which usually occurred at the arrival of a wave node. Following the shearing of the fluid wisp, the disturbance disappeared, and the wisp of fluid was sheared according to the direction of the shear of the next wave trough or crest, and quickly smeared across the density interface such that it was no longer visible. This initial existence of overturning fluid was deemed as the onset of wave breaking; an example of a weakly overturning wisp can be seen in figure 5, at $t/T = 0.375$.

Following this initial instability, the next crest or trough usually became fully unstable to a much more vigorous instability, since the local wave amplitude was increasing slowly in time. At wave crests, disturbances became noticeable slightly ahead of the wave crest, except that these interfacial disturbances then quickly grew and rolled up into the billows resembling those typically associated with the K-H instability. Typically 2–4 billows formed with fairly regular spacing. Billows originating in the wave troughs rolled up in a forward sense (clockwise for a left-to-right travelling wave; $t/T = 0.5, 0.625$), while billows originating in a wave crest rolled up in a backward sense (counter-clockwise for a left-to-right travelling wave; $t/T = 1, 1.125$). This observation is consistent with the orientation of the wave-induced vertical shear at those locations. These billows, like the initial disturbances, were mostly stationary, with only a slight drift in the direction of wave propagation. As the K-H instability is stationary (Hazel 1972; Hogg & Ivey 2003), this drift is perhaps due to the Stokes drift associated with the waves.

Unlike the K-H instability associated with the steady stratified shear layer, where a row of perturbations grow, roll up into billows, and collapse in unison, these billows exhibited spatial variation in their phases due to the spatial variability of the wave shear regulating their growth. Thus, for a row of billows, the leftmost billow (for a wave travelling left to right) could be collapsing while the rightmost billow was just forming, as can be seen in figure 6. In figure 6, the rightmost billow is 'younger', closer to the wave trough, while the leftmost billow has already collapsed and is now being sheared in the opposite direction with the approach of the next wave crest (from the left in the image). In general, billow roll-up was more vigorous, and better organized, in the wave troughs, looking more like the K-H billows usually seen in laboratory experiments on unstable stratified shear layers. However, the core of the billows was usually well-mixed from the initial roll-up, in contrast with the cat's eye patterns of steady shear layers; this may be a consequence of the billows rolling up turbulent fluid from previous collapsed billows. Individual billow growth and collapse was strongly modified by the local temporal variability of the wave shear, which caused billows to abruptly collapse with the passage of wave nodes, regions where the vertical shear is zero. Thus there are important differences between the observed wave instability and the well-studied K-H instability associated with the steady, uniform, stratified shear layer: the spatial and temporal variability of the shear driving the instability in the wave case render the instability itself strongly spatially and temporally variable.

Billow roll-up ceased abruptly just following the arrival of the next wave node, at which point the wave shear begins to reverse direction. The billows quickly collapsed and were smeared horizontally across the interface, leaving small patches of mixed fluid ($t/T = 0.75, 1.25$). For flow visualization experiments in which the index of refraction was not matched, the turbulent stirring produced by these collapsing events was characterized by large shadows in the laser light sheet below the turbulent regions. Even for the experiments with matched index of refraction, the interfacial
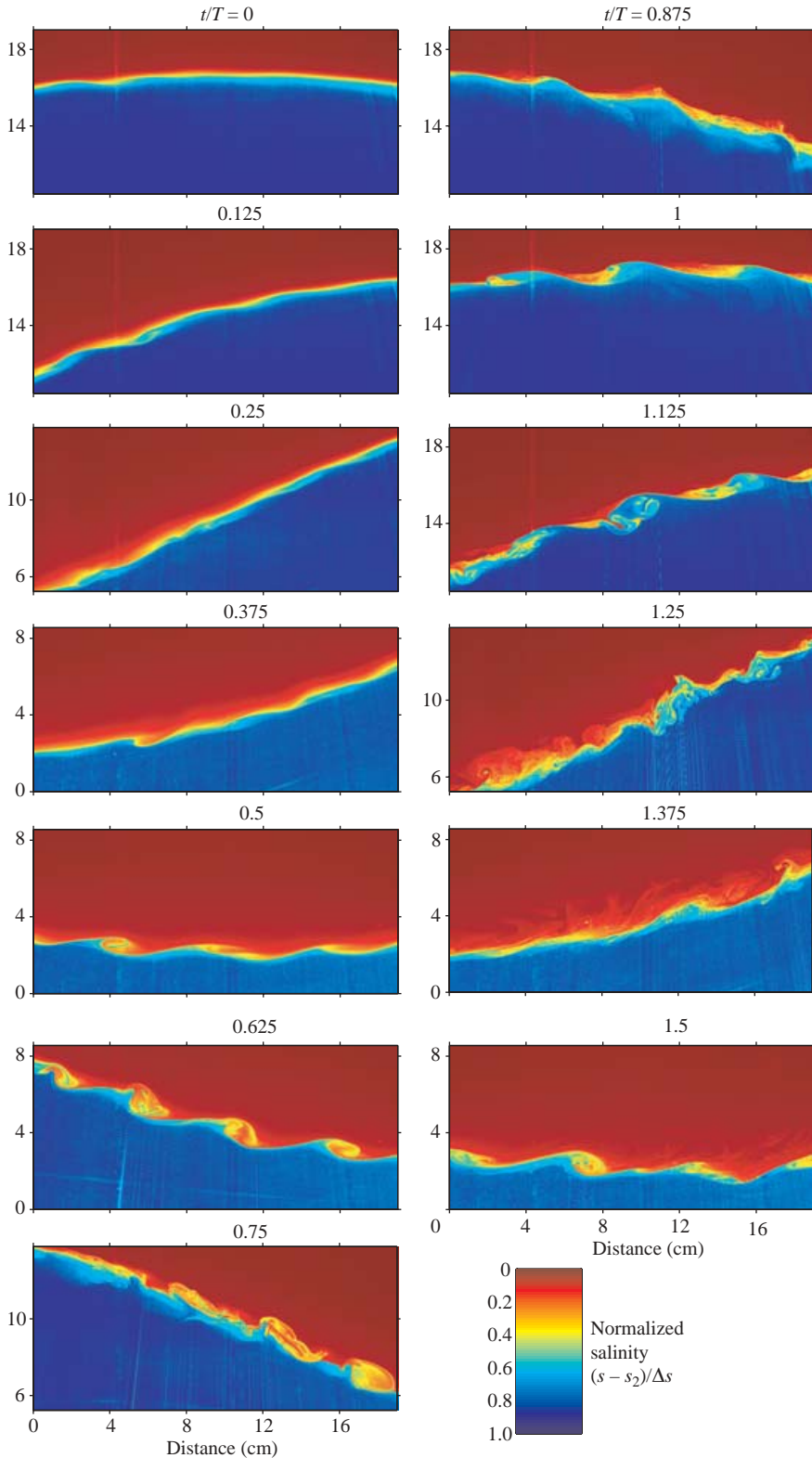
FIGURE 5. Sequence of interfacial wave breaking due to modified Kelvin–Helmholtz instability. Direction of wave propagation is left-to-right, and $k\delta = 0.05$.
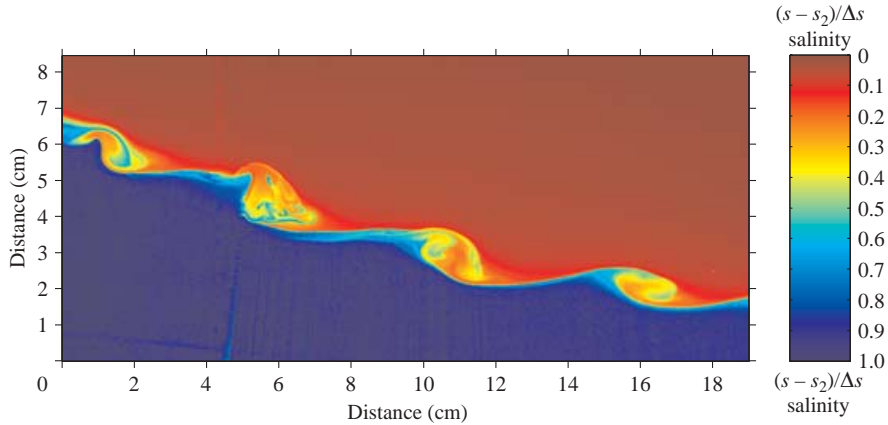
FIGURE 6. Row of Kelvin–Helmholtz billows in wave trough for $k\delta = 0.048$ at time $t/T = 0.625$. The direction of wave propagation is left to right.

stirring associated with the breaking wave was sufficiently vigorous to render small shadows in the light sheet, as can be seen, for example, below the turbulent interface in figure 5, time $t/T = 1.25$. With the arrival of the next wave crest/trough, this collapsed patch of fluid became organized into a billow that then grew as a disturbance, rolled up, and collapsed on the interface. The collapsed turbulent patches seem to form effective perturbation 'seeds' for the next instabilities. Billows at later times were often turbulent from the onset ($t/T = 1, 1.5$), and the clean billow roll-up as observed in many tilting-tube experiments (Thorpe 1968a, 1971, 1973; Atsavapranee & Gharib 1997) was only observed, if at all, in the troughs of waves just starting to break.

After the passage of several waves during which vigorous billow behaviour was observed, the interface became noticeably thickened, and the well-organized rows of billows at wave crests and troughs were no longer observed. In this way, through the local thickening of the density interface, the wave breaking served to return the wave field to a more stable (albeit more chaotic) state than the initial, strongly stratified wavefield. This behaviour is most likely due to an increase in the Richardson number at the wave crests and troughs, since the Richardson number there is proportional to the interfacial thickness (equation (4)). Generally the wave forcing was chosen to allow 3–4 vigorously breaking wave crests or troughs, after which the wavemaker stroke amplitude was quickly ramped off, so that mixing would cease, the wave field would decay, and the interface could then be sharpened for the next experiment.

4.2. Billow structure

4.2.1. Billow development

Typical K-H billow time sequences observed during the experiments using the PLIF flow visualization are shown in figures 7(a) (wave crest) and 7(b) (wave trough). Both figures depict K-H billow development from roll-up to collapse for the case $k\delta = 0.05$. The time between images is approximately $\Delta t = 0.5$ s, which corresponds to $\Delta t/T = 1/16$ (T is the wave period). The spatial extent of the images is labelled in cm. The early, lump-like stage of the instability is not shown.

Figure 7(a) shows the evolution of a typical billow originating at the wave crest. Image (i) shows the billow roll-up before collapse, consistent with the counter-clockwise shear associated with the wave crest for the left-to-right travelling wave. The billow in image (i) exhibits the mixed core that was seen for most of the billows.
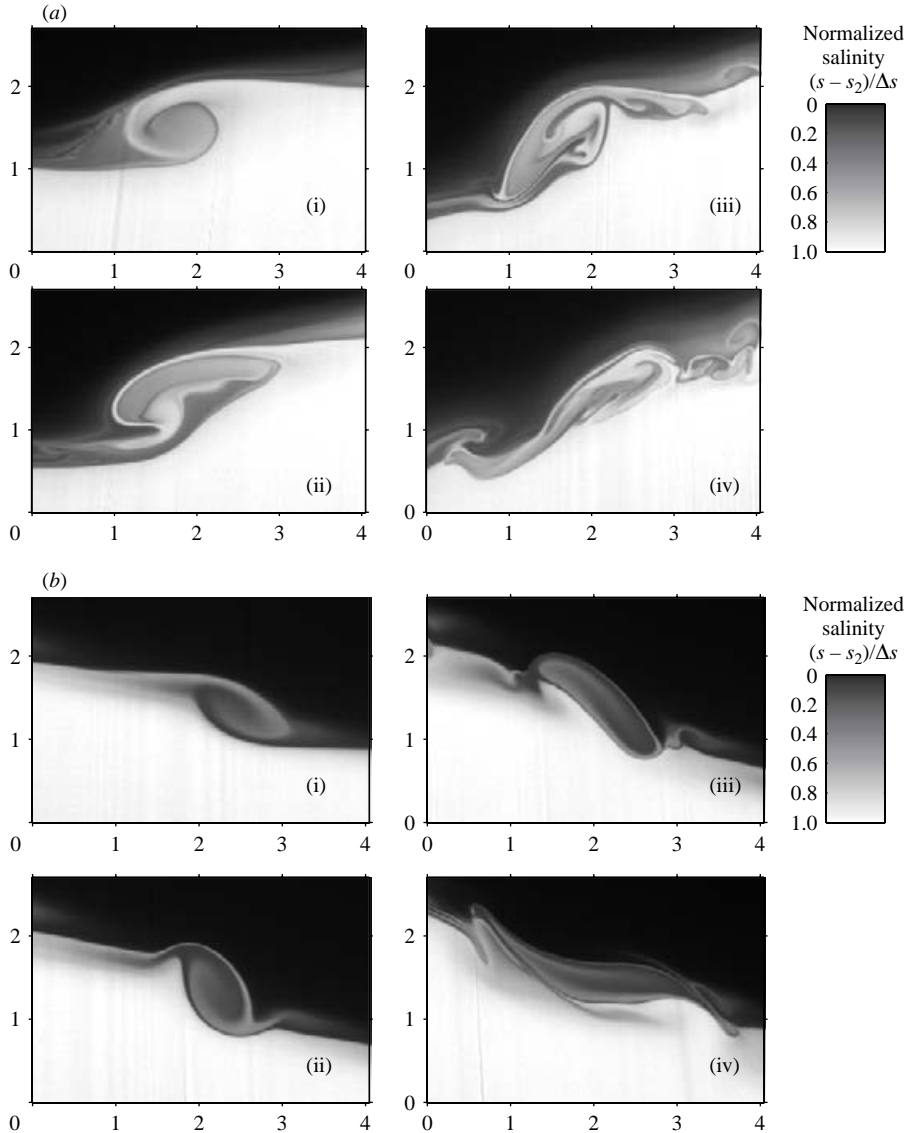
FIGURE 7. Flow visualization of K-H billow sequence originating at (*a*) a wave crest and (*b*) a wave trough for $k\delta = 0.05$. Wave direction is left-to-right, and distance is labeled in cm. The time between images is approximately 0.5 s (0.06T).

This is in contrast to the 'cat's eye' pattern often seen in steady or quasi-steady stratified shear layers. From image (i) it is also apparent that the roll-up is effective in straining the interfacial region into a much thinner interface; measurements show that this straining can often reduce the interfacial thickness locally, both within the billows and between them, from 1.0 cm to as little as 0.2 cm. Simulations of steady stratified shear layers have shown this pre-turbulent straining to be responsible for much of the irreversible mixing that occurs during the K-H instability (Winters *et al.* 1995; Caulfield & Peltier 2000; Smyth, Moum & Caldwell 2001; Peltier & Caulfield 2003), and this may also be true of the wave-induced instability shown here.

Image (ii) in figure 7(a) shows the beginning of the convective collapse and initial straining of the K-H crest billow. At this phase in the wave, the wave-induced shear has ceased, and the K-H billow is gravitationally unstable. Several wave-like disturbances can be seen on the underside of the collapsing billow as the beginning of the convective instability. The fluid inside the billow remains well-mixed, but finer scalar gradients, 1 mm and less in scale, remain at the edges of the collapsing billow. By image (iii) in figure 7a, the crest billow has collapsed and is beginning to be strained across the interface as the wave-induced shear now becomes appreciable in the clockwise direction with the arrival of the next wave trough. The fine-scale structure is still evident, as scalar diffusion has not yet erased the scalar gradients created by the billow roll-up and collapse. Image (iv) in figure 7(a) shows the smeared, collapsed K-H billow that now forms the perturbation for a new K-H billow in the arriving wave trough. The K-H billow is now sheared in the opposite direction, effectively straining the fluid within it and hastening the mixing associated with the small-scale structure remaining from the billow collapse.

Figure 7(b) shows a less vigorous billow that originates in a wave trough. The roll-up seen in image (i) is again consistent with the clockwise shear imparted by the wave at the wave trough; similar to the roll-up of the billow in figure 7(a), the billow core is well-mixed from the onset of the instability. Image (ii) shows the convective collapse of the billow, with the jet formed by the collapse impinging onto the density interface billow, the unstable billow. Sharp scalar gradients remain at this initial stage of collapse, which is not as vigorous as the crest billow shown in figure 7(a).

Image (iii) of figure 7(b) shows the collapsed billow beginning to be strained across the density interface as the wave shear reverses. Sharp contrast still remains between the collapsed billow and the surrounding fluid, but the billow core is now nearly homogenized. Image (iv) shows the result of the continued shearing of the billow, now in the opposite direction from the initial roll-up, leaving it difficult to distinguish from the surrounding interfacial fluid.

As discussed in §4.1, the billows, and the collapsed patches, were observed to drift weakly in the direction of wave propagation. However, the K-H instability is stationary, advecting at the mean interfacial flow speed. While the billow drift is in the direction consistent with the Stokes drift associated with a progressive interfacial wave (Tsuji & Nagata 1973), the Holmboe instability also has a finite speed as it is not a stationary instability. The Stokes drift is of order $(ka)^2 c_p \sim 10^{-2} c_p$, where the interfacial wave speed is $c_p = \omega/k$ and observed steepnesses are $O(10^{-1})$. For a wave-induced Holmboe instability, one would expect propagation speeds of order $10^{-1}(\Delta U/2)$ (Hogg & Ivey 2003), which, with $\Delta U \approx 2a\omega$ also yields a propagation speed of order $10^{-2} c_p$, making the two possible mechanisms difficult to distinguish. The possibility of Holmboe instability is discussed further in §5.

4.2.2. *Billow wavelength*

The wavelengths of the K-H billows, at their initial formation, were determined by manually interrogating the digital images of wave breaking. The value of the billow wavelength for the initial instability was found to be $\lambda_i/\delta = 4.3 \pm 0.9$, where λ_i is the billow wavelength. The noise in the measurement precluded the determination of any dependence of λ_i/δ on the wave Richardson number Ri_w or wavenumber $k\delta$. Measurements of billows at later times in the wave cycle, when the interface had thickened due wave breaking, showed that the billow wavelength was greater for these later times. This suggests that the billow wavelength does indeed grow with the shear layer thickness (which should be the same as the density interfacial thickness, as

discussed in §5), as linear instability theory suggests for the optimum instability (Hazel 1972). The inviscid analysis in §5 suggests that the billow wavelength should be only very weakly dependent on the wave Richardson number for the waves investigated in this study and should scale as $\lambda_i/\delta \approx 2.4$–$2.7$. The billow wavelengths measured by other researches for steady stratified shear layers vary from $\lambda_i/\delta \approx 2.4$ to 5.9 (e.g. Thorpe 1971; Atsavapranee & Gharib 1997). The large discrepancy in the published measurements is caused by differences in the precise definition of the interfacial thickness δ, differing velocity/density interfacial thicknesses, and velocity/density profile offsets.

A possible reason for the discrepancy between the measured wavelength and the theoretical (inviscid) value is viscosity, which would lengthen dominant instability wavelength. Following usual definitions associated with stratified shear layers, the Reynolds number representative of the shear flow near the wave crests and troughs is defined as $Re_0 = \Delta U \delta / 4\nu$, where the parameter ΔU is the total velocity difference across the density interface, and δ is the thickness of the shear layer (e.g. Hogg & Ivey 2003). Re_0 can be approximated for the present wave-induced shear layer as

$$Re_0 \approx \frac{\sqrt{2}(ka)}{4(k\delta)^{1/2}} \left(\frac{g'^{1/2}\delta^{3/2}}{\nu} \right), \qquad (7)$$

where the deep irrotational interfacial wave solutions (e.g. Turner 1973, Ch. 2) have been used to rewrite $\Delta U \approx 2a\omega$ and $\omega^2 = g'k/2$. For the experiments described herein, the quantity $g'^{1/2}\delta^{3/2}/\nu$ was constant at 540, and since measurements to be discussed in §4.3 showed that $ka \approx \sqrt{2k\delta}$ to good approximation at the point of wave breaking, Re_0 was nearly constant for all runs at $Re_0 = 270$. Stratified shear flow stability calculations by Haigh (1995) and Hogg & Ivey (2003) suggest that viscosity begins to affect the stability properties (e.g. billow size and growth rate) for $Re \lesssim 100$, with the effect being to damp high-wavenumber perturbations, shifting the most unstable perturbation to lower wavenumber, and reducing the perturbation growth rates by a few percent. The effects of viscosity are discussed further in §5.

4.3. *Breaking threshold*

The calibrated wave images were used to determine the threshold wave amplitude at which wave breaking occurred. With these flow images, the wave amplitudes were measured, and waves were correspondingly deemed 'stable', at the 'onset of breaking', or 'breaking'. 'Stable' waves were so called because of the absence of any visible deformations of the sinusoidal wave shape aside from those associated with finite-amplitude effects. Waves at the 'onset of breaking' were so called because they exhibited noticeable interfacial disturbances of the type described earlier, in which the interface was perturbed by small-amplitude, nearly stationary lowest-mode interfacial distortions that originated at wave crests and troughs, but disappeared with the arrival of the next wave node. No overturning fluid was observed for waves deemed at the 'onset of breaking'. Waves deemed 'breaking' exhibited visible overturns, in the form of the K-H billows described earlier, which originated in the crests and troughs of the waves.

For a given experiment at a fixed wave frequency, a time sequence of wave images taken at the wave breaking location yielded a record of stable wave amplitudes, wave amplitudes at the onset of breaking, and unstable (breaking) wave amplitudes. The wave amplitudes for the various states are plotted in figure 8, where the measured wave steepness ka is plotted as a function of non-dimensional wavenumber $k\delta$ for the three types of waves measured. Here k has been obtained from the thin-interface,
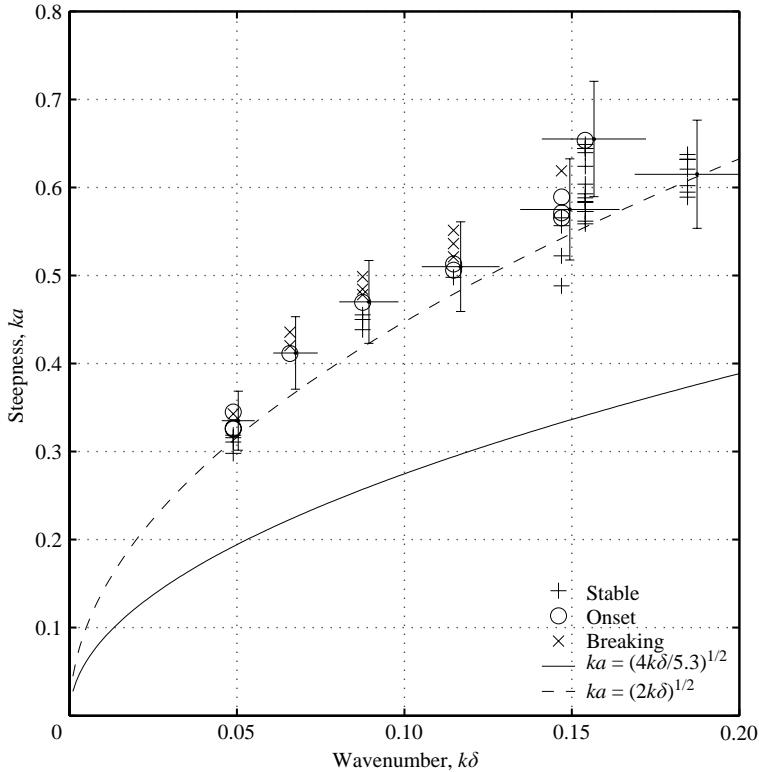
FIGURE 8. Measured wave amplitudes for wave breaking experiments. Also shown are lines of $Ri_w = 1/4$ for two different Ri_w estimates, and error bars for each value of $k\delta$.

two-layer linear dispersion relation

$$\omega^2 = \frac{g'k}{\coth(kh_1) + \coth(kh_2)}. \tag{8}$$

Also plotted are the lines corresponding to $ka = \sqrt{2k\delta}$ and $ka = \sqrt{4k\delta/5.3}$, which result from the application of the steady $Ri = 1/4$ instability criterion to the wave Richardson number Ri_w estimates $Ri_w = k\delta/2(ka)^2$ and $Ri_w = k\delta/5.3(ka)^2$, respectively. From figure 8, it appears that the critical breaking wave steepness ka increases monotonically with $k\delta$, following a $(k\delta)^{1/2}$ dependence that is consistent with the simple application of the steady $Ri = 1/4$ criterion. The data agree very well with the line corresponding to $ka = \sqrt{2k\delta}$; however, this is only a fortuitous coincidence resulting from the offsetting effects of using an overpredictor for Ri_w and the poor assumption that the flow is steady. The effect of unsteadiness is examined more closely in §5.

Figure 9 shows the same onset wave breaking data, plotted in terms of the wave Richardson number Ri_w defined by equation (4). From figure 9, it is apparent that the wave Richardson number at the onset of wave breaking is well below 1/4 for all values of $k\delta$ where wave breaking was observed, in the range $Ri_w = 0.07$–0.08 ± 0.03. It is difficult to discern a trend in Ri_w with $k\delta$ owing to the uncertainty in the measurements, but a possible trend is proposed in the following section.
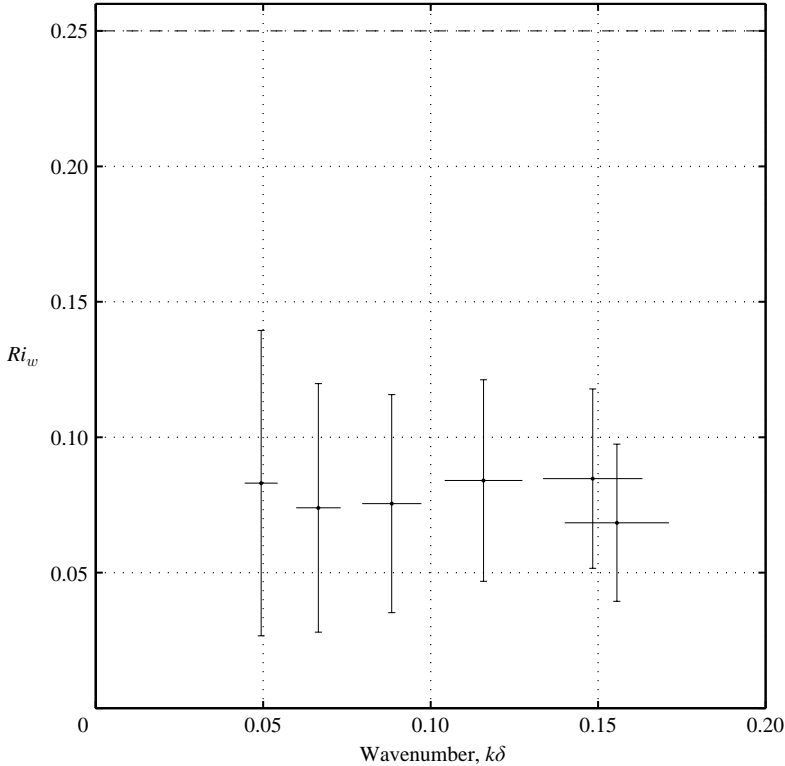
FIGURE 9. Wave Richardson number $Ri_w = k\delta/5.3(ka)^2$ at onset of wave breaking.
Also shown are uncertainty bars.

5. Discussion

The experimental observations described in §4.1 suggest that the instability of long internal waves is strongly temporally and spatially variable, taking the form of an oscillatory stratified shear layer that becomes unstable to a modified Kelvin–Helmholtz instability. To lowest order, the profile of horizontal velocity associated with a lowest-mode internal wave in a hyperbolic tangent stratification at wave crests and troughs (1) is

$$U(z) = a\omega\,\mathrm{sech}^{k/m}(mz)\tanh(mz) \tag{9}$$

Thorpe (1968). This solution represents the lowest-mode inviscid normal-mode solution associated with the hyperbolic tangent density profile (1). An important point here is that for the lowest internal gravity wave mode, the velocity profile is determined by the density profile through the normal-mode relation (e.g. Gill 1982), and thus the density and velocity thicknesses are constrained to be equal for the lowest mode.

The Richardson number distribution associated with (1) and (9) is

$$Ri(z) = Ri_w \frac{[\mathrm{sech}(mz)]^{2(1-k/m)}}{[1 - (k/m + 1)\tanh^2(mz)]^2}. \tag{10}$$

These profiles are plotted in figure 10 for two different wavenumbers.

For long waves ($k/m \longrightarrow 0$), the velocity profile at wave crests and troughs, to lowest order (9), reduces to the oft-studied coincident, equal-thickness hyperbolic tangent stratified shear layer having a total velocity difference $\Delta U = 2a\omega$ across the
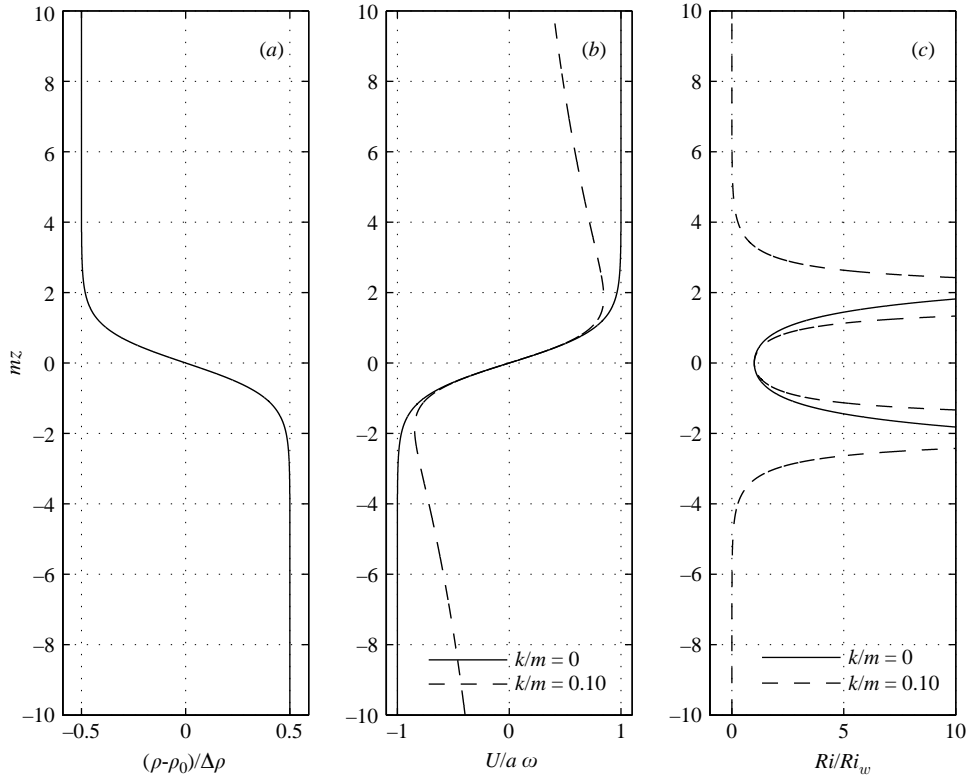
FIGURE 10. Vertical variation of (a) normalized density, (b) horizontal velocity, and (c) Richardson number at wave crests and troughs. Two cases are shown: $k/m = 0, 0.10$ ($k\delta = 0, 0.53$).

shear layer:

$$U(z) = a\omega \tanh(mz). \tag{11}$$

For this profile, the mid-point Richardson number (here termed the wave Richardson number, Ri_w) is the minimum Richardson number in the vertical distribution. From the Miles–Howard Theorem, linear instability is possible for this long-wave case only if the mid-point Richardson number falls below 1/4 (Miles 1961; Howard 1961). However, for waves having higher k/m, the mid-point Richardson number is no longer the minimum Richardson number of the profile (figure 10), and thus the stability of the flow is not guaranteed even if the mid-point Richardson remains above 1/4.

The linear, inviscid stability of this flow, sometimes termed the 'anti-symmetric double jet', was investigated by Hazel (1972). In the long-wave limit ($k/m \to 0$), the flow is potentially unstable to the stationary Kelvin–Helmholtz instability if the mid-point Richardson number (usually termed 'J' for the steady shear layer) falls below 1/4, and stable if the mid-point Richardson number remains above 1/4. The stability boundary in $J - \alpha$ space, with α being the non-dimensional perturbation wavenumber, is given by $J = \alpha(1 - \alpha)$.

From figure 10, it can be seen that the effect of finite k/m (shorter waves) is to make the horizontal velocity in each layer decay with distance away from the interface, similar to that of a surface water wave, but the density and velocity interfacial

thicknesses remain the same. The linear stability of velocity profiles having finite k/m is discussed briefly by Drazin & Howard (1966) and Hazel (1972), who note that the effect of finite k/m is to increase the wavenumber of the most unstable perturbation, changing the stability boundary smoothly from $J = \alpha(1 - \alpha)$ to $J = \alpha^2(3 - \alpha^2)/9$. It is important to note that the instability remains of the stationary K-H type; the critical mid-point Richardson number, below which the flow is potentially unstable, remains at $1/4$.

A number of recent studies have focused on the breakdown of stratified shear layers due to the Holmboe instability (Holmboe 1962), and it is worth briefly discussing the present results in the context of those studies (see Smyth & Winters 2003 for a review). The Holmboe instability typically has lower growth rates than the K-H instability, although simulations have shown that it can generate comparable turbulence and mixing (Smyth & Winters 2003). Holmboe instability can occur, for coincident shear and density tanh profiles, when the velocity thickness exceeds the density thickness by at least 2.4 (Smyth, Klaassen & Pelties 1988; Smyth & Peltier 1989, 1991; Haigh 1995; Smyth & Winters 2003; Hogg & Ivey 2003), and it is believed that this arrangement is probably common in the ocean on account of the differing diffusivities between momentum and the density-stratifying scalars, heat and salt (Smyth & Winters 2003).

To the degree that the hyperbolic tangent velocity (11) and density (1) profiles represent the velocity profile associated with long internal waves, the set equivalence for the velocity and density thicknesses in the present wave-forced case, determined by the normal-mode relation, would seem to preclude the possibility of the Holmboe instability for long progressive internal waves. The stability characteristics of the velocity and density profiles associated with shorter waves, with finite k/m, was investigated by Drazin & Howard (1966) and Hazel (1972), who briefly cite results that the instability remains of the stationary K-H type for the profiles given by (9) and (10). Therefore, it seems that the instability should remain of the K-H type even for shorter waves. Moreover, for the wave breaking reported here, for which the perturbation growth rate must compete with the wave time scale, it seems additionally unlikely that the lower growth rates associated with Holmboe instability would allow the wave-induced instability to form.

Analytical methods do exist to treat the instability of time- and space-varying base flows (see Drazin & Reid 1981 for a review), and these methods, typically Floquet analysis, have been applied to internal gravity waves (e.g. Lombard & Riley 1996; Yau, Klaassen & Sonmor 2004) and to secondary instabilities in stratified and unstratified shear layers (Klaassen & Peltier 1985, 1989, 1991; Smyth & Peltier 1994; Peltier & Caulfield 2003). However, a more common approach is to essentially ignore the spatial or temporal variability when the spatial and temporal scales of the base flow variation are large relative to the instability time scales. Most stability analyses of unsteady or non-uniform stratified shear layers involve the application of the steady, uniform, inviscid Taylor–Goldstein (T-G) equation to find instability growth rates (the reader is referred to excellent discussions on stratified shear layer instability by Turner 1973; Drazin & Reid 1981; and Peltier & Caulfield 2003). For example, Thorpe (1971) treated base flow unsteadiness in unsteady tilting-tube experiments by assuming that the instability growth rates provided by the T-G equation held for slowly varying shear, and that the time-integration of those growth rates would give an indication of instability. The instability of spatially non-uniform stratified shear layers was treated by Pawlak & Armi (1996), who applied the results of the T-G equation for horizontally non-uniform baroclinic exchange flows by assuming that the flow varied little over the region of instability. To our knowledge, the only treatment

of an oscillatory stratified shear layer has been that of Kelly (1965), who examined the problem of an oscillatory shear across a zero-thickness density/velocity interface. Kelly conjectured that the effect of the oscillatory shear, for finite-thickness interfaces, would be to move the most unstable wavenumber to a higher wavenumber and that the effects of the oscillation would be felt mostly by the range of wavenumbers closest to the cutoff wavenumber.

In addition to unsteadiness and non-uniformity, another difference between the present wave instability and a typical stratified shear layer is the vertical acceleration in the wave case. Although the wave motion does oscillate the density/shear interface vertically, with maximum vertical accelerations ($\partial w/\partial t$) at the wave crests and troughs, this vertical acceleration should not affect the development of the instability provided that $\partial w/\partial t \ll g$. Since a progressive interfacial wave has maximum vertical acceleration $\partial w/\partial t \approx a\omega^2$, and for deep waves $\omega^2 \approx g'k/2$, vertical accelerations are negligible provided $(ka)(\Delta\rho/\rho_0) \ll 1$. For these experiments, the quantity $(ka)(\Delta\rho/\rho_0)$ ranged from 0.01 to 0.02, and therefore it is believed that the wave-induced vertical accelerations did not strongly affect the instability. The effect of appreciable vertical wave accelerations is to augment the stabilizing effect of gravity g by an amount $+\partial w/\partial t$ (z positive upward), and thus it is possible that the effect of these accelerations would be destabilizing at the wave crests ($\partial w/\partial t < 0$), and stabilizing in the wave troughs ($\partial w/\partial t > 0$). In our experiments, the only difference observed between trough and crest billows was that the trough billows were slightly more coherent than those originating at wave crests.

Our analysis here is similar to that of Thorpe (1971) in that we assume that the time-integrated T-G instability growth rates should provide an indication of stability for the flow. In §5.1, we apply temporal considerations to the instability, explicitly considering the competition between the instability growth rate and the wave frequency, and determine a wavenumber-dependent theoretical steepness above which long internal waves break. This result is then compared to the data presented earlier in §4.3. In §5.2 we address horizontal non-uniformity and discuss possible reasons for transition to a convective wave instability.

5.1. *Temporal considerations*

In steady stratified shear layers, a non-zero perturbation growth rate is a sufficient criterion for linear instability. However, for the unsteady shear layer, a perturbation may have a non-zero growth rate and the flow may still be stable if the shear is reduced before the perturbation has sufficient time to amplify. Therefore, instability will occur only if sufficient instability growth can occur within the time scale of appreciable shear.

For waves long relative to the interfacial thickness (small k/m), the horizontal velocity profile at wave crests and troughs simplifies to

$$U(x, z, t) = a\omega \tanh(mz) \cos(kx - \omega t). \tag{12}$$

The Richardson number associated with this velocity distribution is

$$Ri(x, z, t) = \frac{N^2}{|\partial U/\partial z|^2}$$

$$= \frac{Ri_w}{\text{sech}^2(mz) \cos^2(kx - \omega t)}, \tag{13}$$

where

$$Ri_w = \frac{k/m}{(ka)^2} \tag{14}$$

is the wave Richardson number, here defined in terms of the hyperbolic-tangent-profile inverse length scale m (equation (3)). Ri_w is the mid-interface Richardson number in the interfacial wave where the shear is greatest, at the crest and troughs of the wave. The vertical variation of crest/trough horizontal velocity (9) and corresponding Richardson number at wave crests and troughs is shown in figure 10 above.

At a given x-location, the mid-interface Richardson number Ri_0 varies in time as

$$Ri_0(t) = \frac{Ri_w}{\cos^2(\omega t)}. \tag{15}$$

If Ri_w is less than $1/4$, then the Richardson number will locally fall below $1/4$ for a time

$$T_w = \frac{2}{\omega} \arccos\left(2Ri_w^{1/2}\right). \tag{16}$$

Wave instability will occur if appreciable instability growth can occur in a time less than T_w. The instability growth rate will determine whether or not appreciable instability growth will occur. Instability growth is parameterized by $a_i(t)$, where $a_i(t)$ is the time-varying amplitude of the growing perturbation, which is presumed to behave as

$$a_i(t) = \frac{1}{\sigma_i}\frac{\mathrm{d}a_i}{\mathrm{d}t}. \tag{17}$$

In a time T_w, the perturbation will grow to an amplitude

$$a_{i_w} = a_{i_0}\exp(\bar{\sigma}_i T_w), \tag{18}$$

where $\bar{\sigma}_i$ is the average growth rate over time T_w and a_{i_0} is the initial perturbation amplitude. Therefore, instability will occur if $a_{i_w}/a_{i_0} \gg 1$, or

$$\bar{\sigma}_i T_w \gg 0. \tag{19}$$

Estimates for the average growth rates of the K-H billows can be obtained from solutions to the T-G equation for steady, coincident hyperbolic tangent velocity and density profiles. Hazel (1972) provided the growth rates for the inviscid K-H instability associated with these profiles. Those results were verified for the present study, and are presented in figure 11. The perturbation growth rates depend on both Ri_0 and the perturbation wavenumber α_i. The optimum instability, that with the highest growth rate, had wavenumber $\alpha_i/m = 0.4$–0.5 that was only weakly dependent on Ri_0. For this optimum wavenumber, the perturbation growth rate was found to increase nearly linearly with decreasing Ri_0. Provided that the crest and trough regions are long relative to this optimum instability size, the optimum instability should prevail. Since the crest and trough regions have length $\pi/2k$, this will be the case provided $k\delta < 0.7$. The dependence of the growth rates on Ri_0 for the optimum instability can be approximated from Hazel's (1972) growth rates as

$$\sigma_i = \frac{m\Delta U}{2}(-0.8Ri_0 + 0.2), \tag{20}$$

where ΔU is the total velocity difference across the hyperbolic tangent shear layer. This approximation correctly prescribes a zero growth rate for the marginal stability case, $Ri_0 = 1/4$. For the velocity profile specified in (12), $\Delta U = 2a\omega$, and therefore the
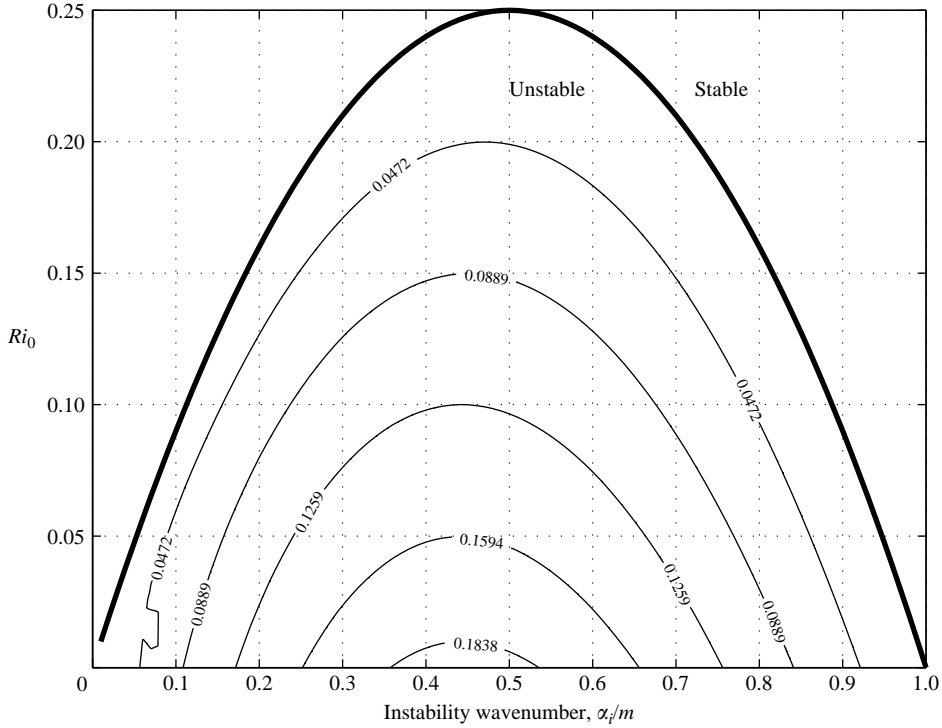
FIGURE 11. Instability growth rate contours ($2\sigma_i/m\Delta U$) from T-G solutions identical to those of Hazel (1972) for coincident hyperbolic-tangent velocity and density profiles. The stability boundary $Ri_0 = \alpha_i(1 - \alpha_i)$ is also shown.

instability growth rates at the crests and troughs of the interfacial waves should relate to the mid-interface Richardson number Ri_0 as

$$\sigma_i = ma\omega(-0.8Ri_0 + 0.2). \tag{21}$$

If the mid-interface Richardson number Ri_0, the controller of instability, varies as $Ri_w/\cos^2(\omega t)$ (equation (15)), then the average growth rate over the time T_w, the time during which the Richardson number is below $1/4$, is

$$\begin{aligned}
\overline{\sigma}_i &= \frac{1}{T_w} \int_{-T_w/2}^{+T_w/2} \sigma_i(Ri_0(t))\, dt \\
&= ma\omega\left[\frac{-0.8Ri_w^{1/2}(1 - 4Ri_w)^{1/2}}{\omega T_w} + 0.2\right],
\end{aligned} \tag{22}$$

and therefore

$$\overline{\sigma}_i T_w = \frac{-0.8Ri_w^{1/2}(1 - 4Ri_w)^{1/2} + 0.4\arccos\left(2Ri_w^{1/2}\right)}{Ri_w^{1/2}(k/m)^{1/2}}. \tag{23}$$

The instability criterion (19) can be rephrased in terms of a constant c for the case of marginal stability as $\overline{\sigma}_i T_w - c = 0$ and solved numerically for different values of c. In general, the value of c will depend on the exact definition of 'instability' since it is directly related to the maximum amplitude of the perturbations (equation (18)). Typically K-H instabilities grow to a buoyancy-regulated amplitude, at which time a
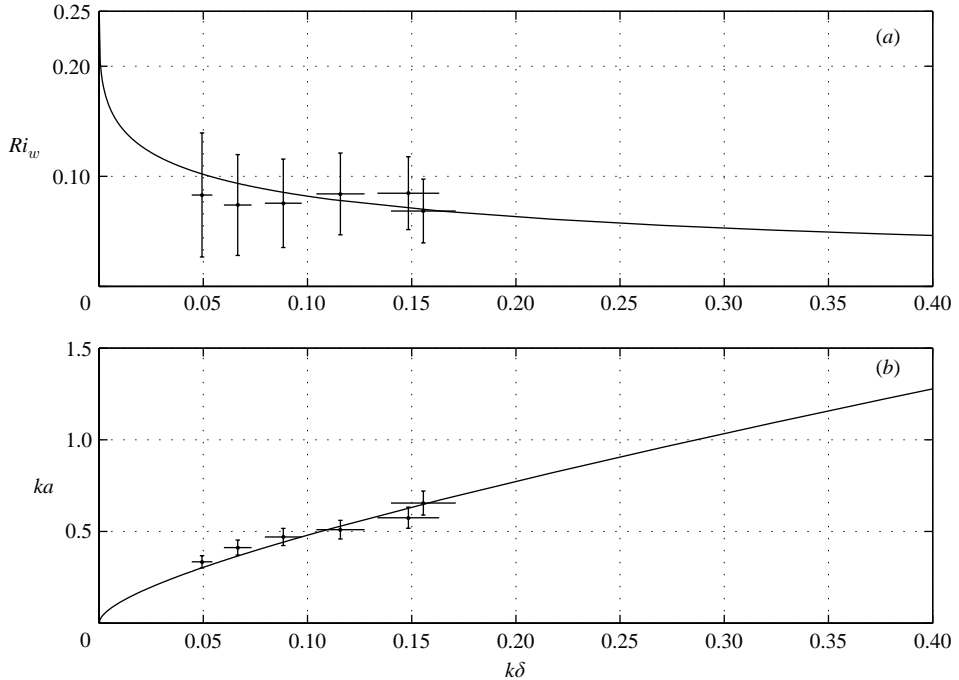
FIGURE 12. Measured critical wave Richardson numbers Ri_w and critical wave steepnesses ka and that predicted by theory (solid line).

catastrophic convective collapse renders the flow fully turbulent (Caulfield & Peltier 2000; Peltier & Caulfield 2003). In §4.3, the wave was deemed 'unstable' when overturning fluid was observed. The solutions to the marginal stability equation give the variation of the critical wave Richardson number Ri_w, below which the wave is expected to break, with the non-dimensional wavenumber k/m (or, equivalently, $k\delta$ via (3)). The results can be rephrased as the critical wave steepness ka by converting Ri_w to ka via equation (14). Figure 12 shows the calculated critical wave Richardson numbers and wave steepnesses along with the data presented earlier in figures 8 and 9; the wavenumber k/m has been converted to $k\delta$ via (3). The value of the constant, $c = 5$, was chosen in order to give good agreement with the data.

Figure 12 shows good agreement between the measured and predicted critical wave Richardson numbers and corresponding steepnesses, correctly predicting the observed $(k\delta)^{1/2}$ dependence for the critical wave steepness ka over the range of the measurements; as mentioned earlier, it is difficult to deduce a trend in the Ri_w values owing to the measurement uncertainty. The analysis correctly predicts a critical wave Richardson number of $1/4$ for the $k\delta = 0$ case, which corresponds to that of the steady stratified hyperbolic-tangent shear layer. As the wavenumber $k\delta$ increases, the theory gives a corresponding reduction in the critical wave Richardson number. This is because higher-frequency waves allow less time for instability growth, necessitating an even lower Richardson number so that the growth rate is sufficiently large.

The theory is expected to fail at higher $k\delta$ for several reasons. First, as $k\delta$ becomes larger (or equivalently as k/m becomes larger), the approximation for the wave crest and trough velocity profile (12) breaks down, owing to both the k/m dependence in (9) and finite-amplitude wave effects that necessitate a higher-order normal-mode solution since the critical steepness ka, the expansion parameter, increases with

$k\delta$. These effects would presumably change the growth rates predicted by the T-G equation, and thus affect the predicted critical Richardson number. Once again, it would have been desirable to use measured simultaneous profiles of velocity and density in the stability calculations, but these were not available from our experiments.

It is expected that viscosity would affect the analysis in several ways. As mentioned earlier, the Reynolds number relevant to the instability, given by (7), was nearly constant for all wave breaking runs at $Re_0 = 270$. Hogg & Ivey (2003) numerically investigated the stability of steady, viscous hyperbolic-tangent stratified shear flows and found that the main effect of viscosity at similar Re_0 is to slightly lower the instability growth rates; the most unstable perturbation wavenumber remains relatively unchanged. Maslowe & Thompson (1971) and Haigh (1995) also obtained similar results, finding that the damping effect of viscosity on the growth rates was restricted to Reynolds numbers less than $O(10^2)$. Since the primary effect of viscosity is to lower the instability growth rates, requiring a lower Richardson number for instability, the viscous effect is difficult to distinguish from the time-scale constraint, which also lowers the critical Richardson number for the wave-induced instability. However, for the Reynolds number of the present experiments, viscosity would account for a lowering of the critical Richardson number by only a few percent from 0.25; the present measurements show an estimated reduction to less than 0.1, making the wave-induced unsteadiness the dominant factor in the observed low critical Richardson numbers. One could presumably follow similar arguments in considering the effects of finite scalar diffusivity on the instability and analysis, although less is known about the effects of scalar diffusivity on stratified shear flow instability.

5.2. *Spatial considerations*

The discussion thus far has essentially dealt with a time-periodic, parallel, uniform, stratified shear flow having a velocity profile corresponding to the long-wave normal-modes solution for hyperbolic-tangent density and velocity profiles. Horizontal non-uniformity has not been considered, although it can be considered in much the way as unsteadiness was examined. If the wave Richardson number is below 1/4, the spatial region at the wave crests and troughs over which the mid-interfacial Richardson number is also below 1/4 is $L_w = (2/k) \arccos(2Ri_w^{1/2})$ since at any instant in time, the mid-interface Richardson number in the wave varies as $Ri_0(x) = Ri_w / \cos^2(kx)$. This region is finite, but presumed not to have much effect on the shear instability provided that L_w is much larger than the optimum instability wavelength $\lambda_i \approx 4\pi/m$; one could apply the T-G equation with inserted Taylor series expansions across a region about the crest and trough regions of the wave. A conjecture is that as $k\delta$ increases, eventually the wave will shorten to a point where L_w becomes of the order of the optimum instability wavelength, and the spatial scale of the instability will be constrained by the wave. If the critical wave steepness behaves as $ka \approx \sqrt{2k\delta}$, which the laboratory data suggest, then the transition $L_w \approx \lambda_i$, where the wave begins to constrain the scale of the instability, will occur at roughly $k\delta \approx 0.8$. Following Hazel's results, associated with this imposed scale of instability is a reduced, less-than-optimum instability growth rate, which will require an even lower Richardson number to satisfy the time-scale instability constraint (19). Hazel's analysis predicts a cutoff wavenumber, $\alpha_i/m = 1$, which is the smallest unstable perturbation; perturbations shorter than $\alpha_i/m = 1$ are not unstable (figure 11). Therefore it is possible that as the wave shortens more and more, eventually shear instability becomes theoretically impossible when the region of appreciable shear (L_w) is less than the smallest permissible instability. Beyond that transition, considering even shorter waves, other instability mechanisms may become

the dominant instability mechanism – perhaps a more classical convective overturning like that of breaking surface waves, and that shown by Fringer & Street (2003) in their numerical simulations of high-$k\delta$ waves. The determination of the exact $k\delta$ value associated with the transition from shear to convective instability – when the smallest permissible shear instability no longer fits within the wave crest and trough regions – would involve calculations of T-G stability diagrams in the $Ri_0 - \alpha_i$-plane for finite ka and $k\delta$ interfacial wave shear/density profiles, such as those given by Thorpe (1968c).

6. Conclusions

Laboratory experiments were conducted in order to determine the wave breaking mechanism and threshold for long interfacial waves with finite-thickness interfaces. For the experiments, monochromatic wave trains with slowly increasing amplitude were forced to breaking through a lateral channel contraction. Flow visualization with planar laser-induced fluorescence (PLIF) allowed the wave breaking mechanism and breaking steepness to be identified. The laboratory experiments have shown that, for waves having wavenumber $0 < k\delta < 0.3$, monochromatic wave breaking occurs due to a shear instability originating in the high-shear regions of the wave crests and troughs. This instability most closely resembles the K-H instability. However, the instability is strongly modified by the temporal and spatial variation of the wave field driving the instability. The initial stages of instability involve the formation and disappearance of low-mode disturbances in the crests and troughs of the wave; these disturbances sometimes released faint wisps of fluid into the upper layer as the wave neared the breaking amplitude.

The full wave instability initially resembles the K-H instability in a stratified shear layer, with several disturbances forming in the crest and trough regions rolling up into finite-amplitude billows. The sense of billow roll-up is consistent with the sense of shear, respectively, at the wave crests and troughs. The billows are nearly stationary, but do have a slow drift in the direction of wave propagation, consistent with the Stokes drift for finite-amplitude progressive interfacial waves. While we believe that the instability is an unsteady, non-uniform K-H instability, more detailed stability analysis is required to prove this conclusively; measurements permitting such analysis were not available for our study. The subsequent collapse of these billows, unlike an unstable steady stratified shear layer, appears to be regulated not by buoyancy but by the change in direction of the wave shear caused by local changes in wave phase. The collapsed billows are quickly sheared across the interface, and these patches form effective perturbations in the next wave crest or trough; these patches then again roll up into billows that are more turbulent and disorganized. The cycle continues, in the experiments, until the interface has thickened to a stable state for the wave conditions, or until wave generation is stopped. Future work will focus on the analysis of the billow growth rates and wavelengths in the light of what is already known about steady stratified shear layer instability.

The critical steepness at which wave breaking occurred was determined using visual measurements of the wave crests and troughs at wave breaking. The results show that the critical steepness, for the range of waves studied here, is wavenumber-dependent, with the breaking steepness increasing with increasing wavenumber as $ka \approx \sqrt{2k\delta}$ to good approximation. This is consistent with a critical Richardson number regulating wave instability. However, the wave Richardson number Ri_w calculated from the observations at the threshold of wave breaking was significantly below the often-assumed stability limit of 1/4. The measured estimates of the wave Richardson number

were found to be $Ri_w = 0.07$–0.08 ± 0.03 at the initial observation of overturning. This is not unexpected, as the stability limit $Ri_w = 1/4$ is derived for steady flows for which the instability has unlimited time to develop. In the case of instability arising due to wave-induced shear, the applied shear driving the instability is oscillatory, and thus to become unstable, the flow perturbations must not only have a non-zero instability growth rate; they must also have a growth rate large enough such that the perturbations grow to finite amplitude within the wave time scale.

A simple hypothesis to predict the wavenumber dependence of the steepness at which interfacial waves will break was put forth. The hypothesis relies on growth rates provided by solutions to the T-G equation for a hyperbolic-tangent stratified shear layer, a flow which is taken to model the flow at the crests and troughs of progressive long interfacial waves. These growth rates were used to quantify the wave instability threshold in terms of ka or Ri_w. The prediction is based on the requirement that appreciable instability growth take place over the time of wave-imposed shear. For waves having crest and trough regions much greater than the optimum instability wavelength ($k\delta \lesssim 0.8$), the instability is expected to be the optimum instability (that with the highest growth rate). In this case, the instability wavelength should scale only with the interfacial thickness, in keeping with inviscid stratified shear layer analysis, and be nearly independent of Richardson number (the interfacial thickness was not varied in this study). In this regime, the long-wave regime, the theory correctly predicts a Richardson number below $1/4$ at wave breaking, a corresponding increase in wave breaking threshold steepness with increasing number, and shows good agreement with the laboratory data when a constant used in the argument is chosen appropriately. The theory is expected to fail at higher $k\delta$ owing to finite-amplitude and viscous effects that would change the underlying base flow assumed in the stability analysis.

It is hypothesized that, as $k\delta$ increases, eventually the wave crest and trough regions shorten to a scale that is comparable with the optimum instability wavelength. Beyond this point, the wave may set the scale of the instability, the instability will be less than optimum, and thus the critical wave steepnesses and critical wave Richardson numbers will change more dramatically with $k\delta$. Stratified shear instability theory predicts a cutoff perturbation wavenumber above which no unstable perturbations exist. Therefore it is possible that a corresponding cutoff wavenumber exists for the shear instability of progressive interfacial waves, occurring when the wavenumber $k\delta$ increases to the point where the crest and trough regions of the wave are smaller than the smallest permissible instability. Beyond this point, the instability may transition to a more classical convective wave breaking similar to that found by Fringer & Street (2003) in their experiments of higher-$k\delta$ waves.

REFERENCES

ALAYHARI, A. & LONGMIRE, E. K. 1994 Particle image velocimetry in a variable density flow: application to a dynamically evolving microburst. *Exps. Fluids* **17**, 434–440.

ANTENUCCI, J. P. & IMBERGER, J. 2001 On internal waves near the high frequency limit in an enclosed basin. *J. Geophys. Res.* **106**, 22465–22472.

ATSAVAPRANEE, P. & GHARIB, M. 1997 Structures in stratified plane mixing layers and the effects of cross-shear. *J. Fluid Mech.* **342**, 53–86.

BOEGMAN, L., IMBERGER, J., IVEY, G. N. & ANTENUCCI, J. P. 2003 High-frequency internal waves in large stratified lakes. *Limnol. Oceanogr.* **48**, 895–919.

CAULFIELD, C. P. & PELTIER, W. R. 2000 The anatomy of the mixing transition in homogeneous and stratified free shear layers. *J. Fluid Mech.* **413**, 1–47.

DAVIERO, G. J., ROBERTS, P. J. W. & MAILE, K. 2001 Refractive index matching in large-scale stratified experiments. *Exps. Fluids* **31**, 119–126.

DAVIS, R. E. & ACRIVOS, A. 1967 The stability of oscillatory internal waves. *J. Fluid Mech.* **30**, 723–736.

DRAZIN, P. G. & HOWARD, L. N. 1966 Hydrodynamic stability of parallel flow of inviscid fluid. *Adv. Appl. Mech.* **9**, 1–89.

DRAZIN, P. G. & REID, W. H. 1981 *Hydrodynamic Stability*. Cambridge University Press.

FRINGER, O. B. & STREET, R. L. 2003 The dynamics of breaking progressive interfacial waves. *J. Fluid Mech.* **494**, 319–353.

FRITTS, D. C. 1989 A review of gravity wave saturation processes, effects, and variability in the middle atmosphere. *PAGEOPH* **130** (2), 343–371.

FRITTS, D. C., ISLER, J. R., HECHT, J. H., WALTERSCHEID, R. L. & ANDREASSEN, Ø. 1997 Wave breaking signatures in OH airglow and sodium densities and temperatures, 2, simulation of wave and instability structures. *J. Geophys. Res.* **102**, D6, 6669–6684.

GILL, A. E. 1982 *Atmosphere-Ocean Dynamics*. Academic.

GREGG, M. C. 1987 Diapycnal mixing in the thermocline: a review. *J. Geophys. Res.* **92**, 5249–5286.

GREGG, M. C., WINKEL, D. P. & SANFORD, T. B. 1993 Varieties of fully resolved spectra of vertical shear. *J. Phys. Oceanogr.* **23**, 124–141.

GRUE, J., A. JENSEN, A., RUSAS, P. & SVEEN, J. K. 2000 Breaking and broadening of internal solitary waves. *J. Fluid Mech.* **413**, 181–217.

HAIGH, S. P. 1995 Non-symmetric Holmboe Waves. PhD thesis, University of British Columbia.

HAZEL, P. 1972 Numerical studies of the stability of inviscid stratified shear flows. *J. Fluid Mech.* **51**, 39–61.

HECHT, J. H., WALTERSHEID, R. L., FRITTS, D. C., ISLER, J. R., SENFT, D. C., GARDNER, C. S. & FRANKE, S. J. 1997 Wave breaking signatures in OH airglow and sodium densities and temperatures 1. airglow imaging, na lidar, and MF radar observations. *J. Geophys. Res.* **102**, D6, 6655–6668.

HODGES, B. R., IMBERGER, J., SAGGIO, A. & WINTERS, K. B. 2000 Modeling basin-scale internal waves in a stratified lake. *Limnol. Oceanogr.* **45**, 1603–1620.

HOGG, A. McC. & IVEY, G. N. 2003 The Kelvin-Helmholtz to Holmboe instability transition in stratified exchange flows. *J. Fluid Mech.* **477**, 339–362.

HOLMBOE, J. 1962 On the behaviour of symmetric waves in stratified shear layers. *Geophys. Publ.* **24**, 67–113.

HOLYER, J. Y. 1979 Large amplitude progressive interfacial waves. *J. Fluid Mech.* **93**, 433–448.

HOWARD, L. N. 1961 Note on a paper of John W. Miles. *J. Fluid Mech.* **10**, 509–512.

KELLY, R. E. 1965 The stability of an unsteady Kelvin-Helmholtz flow. *J. Fluid Mech.* **22**, 547–560.

KLAASSEN, G. P. & PELTIER, W. R. 1985 The onset of turbulence in finite-amplitude Kelvin-Helmholtz billows. *J. Fluid Mech.* **155**, 1–35.

KLAASSEN, G. P. & PELTIER, W. R. 1989 Role of transverse secondary instabilities in the evolution of free shear layers. *J. Fluid Mech.* **202**, 367–402.

KLAASSEN, G. P. & PELTIER, W. R. 1991 Influence of stratification on secondary instability in free shear layers. *J. Fluid Mech.* **227**, 71–106.

LIN, C.-L., FERZIGER, J. H. KOSEFF, J. R. & MONISMITH, S. G. 1993 Simulation and stability of a two dimensional internal gravity wave in a stratified shear flow. *Dyn. Atmos. Oceans* **19**, 325–366.

LOMBARD, P. N. & RILEY, J. J. 1996 Instability and breakdown of internal gravity waves. I. Linear stability analysis *Phys. Fluids* **8**, 3271–3287.

LONG, R. R. 1972 The steepening of long internal waves. *Tellus* **24**, 88–99.

MASLOWE, S. A. & THOMPSON, J. M. 1971 Stability of a stratified free shear layer. *Phys. Fluids* **14**, 453–458.

McDougall, T. J. 1979 On the elimination of refractive-index variations in turbulent density-stratified liquid flows. *J. Fluid Mech.* **93**, 83–96.

Michallet, H. & Barthelemy, E. 1997 Ultrasonic probes and data processing to study interfacial solitary waves. *Exps. Fluids* **22**, 380–386.

Michallet, H. & Ivey, G. N. 1999 'Experiments on mixing due to internal solitary waves breaking on uniform slopes. *J. Geophys. Res.* **104**, 13467–13477.

Miles, J. W. 1961 On the stability of heterogeneous shear flows. *J. Fluid Mech.* **10**, 496–508.

Orlanski, I. & Bryan, K. 1969 Formation of the thermocline step structure by large-amplitude internal gravity waves. *J. Geophys. Res.* **74**, 6975–6983.

Pawlak, G. & Armi, L. 1996 Stability and mixing of a two-layer exchange flow. *Dyn. Atmos. Oceans* 139–151.

Peltier, W. R. & Caulfield, C. P. 2003 Mixing efficiency in stratified shear flows. *Annu. Rev. Fluid Mech.* **35**, 135–167.

Phillips, O. M. 1966 *Dynamics of the Upper Ocean.* Cambridge University Press.

Ramberg, S. E. & Griffin, O. M. 1987 Laboratory study of steep and breaking deep water waves. *J. Waterway, Port, Coast., Ocean Engng* **113**, 493–506.

Scinocca, J. F. 1995 The mixing of mass and momentum by Kelvin-Helmholtz billows. *J. Atmos. Sci.* **52**, 2509–2530.

Smyth, W. D., Klaassen, G. P. & Peltier, W. R. 1988 Finite amplitude Holmboe waves. *Geophys. Astrophys. Fluid Dyn.* **43**, 181–222.

Smyth, W. D., Moum, J. N. & Caldwell, D. R. 2001 The efficiency of mixing in turbulent patches: Inferences from direct simulations and microstructure observations. *J. Phys. Oceanogr.* **31**, 1969–1992.

Smyth, W. D. & Winters, K. B. 2003 Turbulence and mixing in Holmboe waves. *J. Phys. Oceanogr.* **33**, 694–711.

Smyth, W. D. & Peltier, W. R. 1989 'The transition between Kelvin-Helmholtz and Holmboe instability: An investigation of the overreflection hypothesis. *J. Atmos. Sci.* **46**, 3698–3720.

Smyth, W. D. & Peltier, W. R. 1991 Instability and transition in Kelvin-Helmholtz and Holmboe waves. *J. Fluid Mech.* **228**, 387–415.

Smyth, W. D. & Peltier, W. R. 1994 Three-dimensionalization of barotropic vortices on the f-plane. *J. Fluid Mech.* **265**, 25–64.

Staquet, C. & Sommeria, J. 2002 Internal gravity waves: From instabilities to turbulence. *Annu. Rev. Fluid Mech.* **34**, 559–593.

Stastna, M. & Lamb, K. G. 2002 Large fully nonlinear internal solitary waves: The effect of background current. *Phys. Fluids* **14**, 2897–2999.

Stokes, G. G. 1849 On the theory of oscillatory waves. *Trans. Camb. Phil. Soc.* **8**, 441–455.

Thorpe, S. A. 1966 On wave interactions in a stratified fluid. *J. Fluid Mech.* **24**, 737–751.

Thorpe, S. A. 1968a A method of producing a shear flow in a stratified fluid. *J. Fluid Mech.* **32**, 693–704.

Thorpe, S. A. 1968b On standing internal gravity waves of finite amplitude. *J. Fluid Mech.* **32**, 489–528.

Thorpe, S. A. 1968c On the shape of progressive internal waves. *Phil. Trans. R. Soc. Lond.* A **263**, 563–613.

Thorpe, S. A. 1971 Experiments on the instability of stratified shear flows: Miscible fluids. *J. Fluid Mech.* **46**, 299–319.

Thorpe, S. A. 1973 Experiments on instability and turbulence in a stratified shear flow. *J. Fluid Mech.* **61**, 731–751.

Thorpe, S. A. 1975 The excitation, dissipation, and interaction of internal waves in the deep ocean. *J. Geophys. Res.* **80**, 328–338.

Thorpe, S. A. 1978 On the shape and breaking of finite amplitude internal gravity waves in a shear flow. *J. Fluid Mech.* **85**, 7–31.

Thorpe, S. A. 1987 Transitional phenomena and the development of turbulence in stratified fluids: A review. *J. Geophys. Res.* **92**, C5, 5231–5248.

Troy, C. D. 2003 The breaking and mixing of progressive internal waves. PhD thesis, Stanford University.

Troy, C. D. & Koseff, J. R. 2005 The generation and quantitative visualization of breaking internal waves. *Exps. Fluids* **38**, 549–562.

Tsuji, Y. & Nagata, Y. 1973 Stokes' expansion of internal deep water waves to the fifth order. *J. Oceanogr. Soc. Japan* **29**, 61–69.

Turner, J. S. 1973 *Buoyancy Effects in Fluids*. Cambridge University Press.

Wessels, F. & Hutter, K. 1996 Interaction of internal waves with a topographic sill in a two-layered fluid. *J. Phys. Oceanogr.* **26**, 5–20.

Winters, K. B. & D'Asaro, E. A. 1994 Three-dimensional wave instability near a critical level. *J. Fluid Mech.* **272**, 255–284.

Winters, K. B., Lombard, P. N., Riley, J. J. & D'Asaro, E. A. 1995 Available potential energy and mixing in density-stratified fluids. *J. Fluid Mech.* **289**, 115–128.

Woods, J. D. 1968 Wave induced shear instability in summer thermocline. *J. Fluid Mech.* **32**, 791–800.

Yau, K.-H., Klaassen, G. P. & Sonmor, L. J. 2004 Principle instabilities of inertio-gravity waves. *Phys. Fluids* **16**, 936–951.